Energy Storage Materials 10 (2018) 160–167

Contents lists available at ScienceDirect

Energy Storage Materials

journal homepage: www.elsevier.com/locate/ensm

MnO quantum dots embedded in carbon nanotubes as excellent anode for lithium-ion batteries

Lijun Zhang[a], Guanglin Xia[a], Yuqin Huang[a], Chenyun Wei[a], Yiwei Yu[b], Dalin Sun[a], Xuebin Yu[a,*]

[a] Department of Materials Science, Fudan University, Shanghai, China
[b] Department of physics, Arizona State University, Tempe, AZ, USA

ARTICLE INFO

Key words:
MnO quantum dots
Porous carbon nanotubes
Porogen reagent
Lithium-ion batteries

ABSTRACT

MnO quantum dots homogenously embedded in carbon nanotubes (denoted as MnO QDs@CNTs) were prepared via a scalable electrospinning technique with LiN_3 serving as poregen agent. The strong N_2 evolution resulting from the explosive decomposition of the porogen LiN_3 and oxidation diffusion of $MnCl_2$ during the heat treatment are found to be responsible for the formation of the hierarchy structure. As binder-free anodes, the composite networks displayed extraordinary LIBs performance with good reversible capacity (as high as ~1100 mAh g^{-1} at 100 mA g^{-1}), high coulombic efficiency, outstanding rate capability and superior cyclic performance (nearly no capacity fading after 200 cycles at a high current density of 3000 mA g^{-1}), owing to the unique combination of ultra-small MnO QDs and stable CNTs with excellent transport properties. This shows MnO QDs@CNTs composites are almost the most efficient MnO-based anode materials for LIBs so far.

1. Introduction

Rechargeable lithium ion batteries (LIBs) have attracted intensive attention during the past decade [1]. Tt is urgent to design and fabricate high reversible capacity, long cycle-life and low cost LIBs electrode materials [2,3]. Because of the high theoretical specific capacities, transition metal oxides M_xO_y (M=Co, Fe, Sn, Ni and Mo etc) [4–7] have been intensively exploited as promising anode materials, recently [8]. Due to the low conversion potential and voltage hysteresis (< 0.8 V), high density (5.43 g cm^{-3}), low cost, environmental benignity, and the high abundance of Mn, MnO is an attractive anode material among the various transition metal oxides investigated for LIBs [9,10]. However, the poor cycling stability and inferior rate capability are major challenges in the application of MnO to practical LIBs [11]. During the repeated lithium insertion/extraction processes, the drastic volume changes give rise to pulverization, which results in the electrical connection of such anode materials breaking from current collectors and rapid capacity fading upon cycling.

To figure out these issues, considerable efforts have been made to improve the structural stability and integrity of MnO anodes [12]. Two strategies are believed feasible. On the one hand, coating or hybridizing MnO materials with advanced carbon nano materials [13], which could effectively enhance the power and energy densities and initially improve the stability [14,15], because carbon nanomaterials can greatly strengthen the conductivity of MnO, and besides, the elastic feature of carbon materials relieve the strain availably caused by the volumetric change during lithiation/delithiation process, partly improving their cycling stability. These hybrid methods have been demonstrated on the synthesis of MnO/C core/shell nanorods [16], MnO nanoparticles (NPs) attached on grapheme [14] and hollow porous MnO/C microspheres [17], *etc.* On the other hand, reducing the size of the particles to the nanoscale is also helpful [10]. According to $\tau = L^2D^{-1}$ (where τ is the diffusion time, L is the diffusion length and D is the diffusion constant) [18,19], smaller particles exhibit faster Li^+ diffusion and better capability for lithium storage. Simultaneously, they can significantly reduce the absolute volume variation and provide larger electrode/electrolyte interface for high rate performance.

Quantum dots (QDs) [20], as a result of their unique physical properties, which arise due to the quantum confinement effect, have potential in nanoscale device applications generally [21] such as next-generation electronic and optoelectronic devices (including LEDs and solar cells) [22]. So far, many metal oxide [23] QDs have been synthesized and showed excellent electrochemical performances [24] as electrode materials for LIBs [25,26] because of the small particle size and good dispersion [27] (e.g., down to several nanometers [28]) which endow the composite electrode superior high surface area to buffer the volume change of the particles thus facilitates the transport kinetics [29]. However, to the best of our knowledge, there has been no report on the synthesis of MnO QDs for LIBs electrodes.

Herein, we demonstrated a new process for the facile synthesis of

* Corresponding author.
E-mail address: yuxuebin@fudan.edu.cn (X. Yu).

http://dx.doi.org/10.1016/j.ensm.2017.01.007
Received 30 September 2016; Received in revised form 12 January 2017; Accepted 15 January 2017
Available online 16 January 2017

novel heterostructured MnO QDs@CNTs by electrospinning with LiN_3 serving as porogen agent followed by step-wise thermal treatment. The phase separation between LiN_3 and $MnCl_2$ coupled with strong evolution of N_2 resulting from the explosive decomposition of LiN_3 in the center of naonfibers (NFs) during the heat treatment are responsible for the formation of the MnO QDs@CNTs. The N_2 released from the decomposition of the porogen LiN_3 can function as separators to prevent the agglomeration of MnO nanocrystals resulting in the formation of the sub-5nm MnO QDs. By comparison, MnO nanoparticles (MnO NPs) with sizes of 40–50 nm were synthesized in the carbon NFs during the calcination of electrospund NFs without the presence of LiN_3 (denoted as MnO NPs@CNFs). Compared to other reported MnO/C nanocomposites, our sub-5-nm MnO QDs@CNTs can further improve Li^+ insertion by weakening diffusion/migration barrier, allowing easy penetration of the electrolyte between neighboring NPs and hence overcoming internal resistance, which is perfect for high energy/power applications. Moreover, CNTs matrices with high electric conductivity could provide extra "cushion" to suit large volume change of MnO QDs during cycling charge and discharge process. Benefiting from the unique structural features, MnO QDs@CNTs shows significantly enhanced electrochemical properties as anode materials for LIBs compared to MnO NPs@CNFs and bulk MnO.

2. Materials and methods

2.1. Synthesis for the anode material

2.1.1. MnO QDs@CNTs

Poly(vinyl alcohol) (0.5 g, Alfa Aesar, Mv=88,000) was mixed with deionized water (5 mL) and stirred in water bath at 90 °C for 8 h to make PVA solution. After cooling down to room temperature, LiN_3 solution (0.4 mL, 20 wt.%) in water and $MnCl_2$ (75 mg, Sigma) was then added and vigorously stirred for 6 h to make a homogeneous spinning dope. The resultant precursor solution was poured into a syringe with a 18-gauge blunt tip needle. The flow rate of solution was approximately 300 μL h^{-1} controlled by a syringe pump (Longer, TJP-3A, China), and a grounded stainless steel plate was horizontally placed 15 cm from the needle to collect the nanowires. A high voltage of 16 kV was applied by a high-voltage power supply. The as-collected electrospun fibers were firstly dewatered at a temperature of 75 °C under dynamic vacuum for 15 h and then calcined at 550 °C for 3 h (heating rate: 2 °C min^{-1}) under dynamic N_2 atmosphere to obtain the MnO QDs@CNTs.

2.1.2. MnO NPs@CNTs

The MnO NPs@CNFs was synthesized by the same method as the MnO QDs@CNFs except LiN_3 addition.

2.2. The assembly of LIBs batteries

The MnO QDs@CNTs and MnO NPs@CNFs networks were directly used as binder-free anodes. For the bulk MnO, carbon black, and poly(vinyl difluoride) (PVDF) were mixed in NMP with a weight ratio of 80:10:10, and then the slurry was pasted onto pure Cu foil. The electrolyte consists of asolution of 1 M $LiPF_6$ in ethylene carbonate (EC)/dimethyl carbonate (DMC) (volumeratio of 1:1). Pure lithium foil was used as counter electrode, and the separator was a polypropylene membrane from Celgard. The coating thickness on Cu foil is about 100 μm. The mass loading of the active materials is about 1 mg. The cells were assembled in an argon filled glovebox.

2.3. Characterization of material and discharge products

The high-resolution synchrotron powder X-ray diffraction data were collected by a Mythen-II detector with a wavelength of λ=1.0315 Å at the Powder Diffraction Beamline, Australian Synchrotron. Nitrogen absorption/desorption isotherms (Brunauer–Emmett–Teller (BET) technique) at the temperature of liquid nitrogen via a Quantachrome NOVA 4200e instrument were collected to characterize the pore structure of the samples. The crystalline phase of the samples also was detected by X-ray photoelectron spectroscopy (XPS, Surface Science Instruments S-probe spectrometer). Raman spectrum was recorded at ambient temperature with a NEXUS 670 FT-IR Raman spectrometer. Thermal property measurements were performed by thermogravimetry (TG, STA 409C) with a heating rate of 10 °C min^{-1} under air. The microstructures were observed by transmission electron microscopy (TEM, JEM-2100F, JEOL) and field-emission scanning electron-microscopy (SEM, S-4800, Hitachi).

2.4. Electrochemical measurements

Electrochemical measurements were performed using coin type 2032 cells. The charge and discharge performances were carried out on a LAND-CT2001C test system within a range of 0.001–3 V at different current densities. Cyclic voltammogram experiment was performed on an Autolab PGSTAT302N electro chemical workstation at a scan rate of 0.1 mV s^{-1}.

3. Results and discussion

As a binder-free anode, the MnO QDs@CNTs composite was fabricated in three consecutive steps as shown in Fig. 1. Briefly, a sol–gel composed of PVA, LiN_3 and $MnCl_2$ in deionized water was prepared and electrospun on a copper foil. The obtained films were dried for 24 h in vacuum at 75 °C and then annealed in a N_2 flow at 550 °C for 3 h with a heating rate of 2 °C min^{-1}. The digital photos of the dried $MnCl_2$-LiN_3/PVA and the obtained MnO QDs@CNTs films (Fig. S1 in the ESI†) displayed that the MnO QDs@CNTs film with a diameter of 1.5 cm and a thickness of 140 um (Fig. S2†) is intact without any crack, revealing the robust structure of the networks and its promising future in LIBs as a binder-free anode. The morphology and microstructure of the as-prepared $MnCl_2$-LiN_3/PVA NFs and the as-obtained MnO QDs@CNTs were further characterized by scanning electron microscope (SEM, Fig. S3†) and transmission electron microscopy (TEM). It can be found from Fig. S3† that the as-prepared $MnCl_2$-LiN_3/PVA NFs are randomly oriented with lengths of several hundreds of micrometers. A high magnification in Fig. 2a illustrates that these $MnCl_2$-LiN_3/PVA NFs are smooth-faced with a diameter of ~220 nm. After carbonization in N_2 at 550 °C (Fig. 2b and S3†), the diameter of the obtained MnO QDs@CNTs decreases to 160 nm and the surface becomes less smooth with many micropores appearing on the surfaces (Fig. S4†), which could be attributed to the decomposition of PVA and the shrinkage of the NFs upon partial sintering [30]. The inset of Fig. 2b gives a magnified cross section of MnO QDs@CNTs, revealing the hollow interior nature of these tubular structures. The thickness of the tube walls is around 40 nm, as shown in Fig. 2c, the TEM detailed that the long continuous nanotubes are hollow, which is corresponding to the SEM observation. The nanotube structure provides superb merits as an anode materials such as (i) the static outer surface gives rise to a stable SEI; (ii) the existence of inner space is benefit to transmission of Lithium ion and allows for free volume expansion of the MnO QDs without mechanical damage. The high magnification TEM image (Figs. 2d and 2e) reveal that uniform MnO QDs (black dots) with an average particle size of ~3.6 nm were well dispersed in the carbon matrices. The selected-area electron diffraction (SAED) pattern (inset of Fig. 2e) demonstrates the poor crystallinity of the MnO QDs. The lattice spacing is measured to be 0.26 nm as shown in Fig. 2f corresponding to the (111) interplanar distance of the MnO phase. Figs. 2g and 2h are the SEM and TEM images of the MnO NPs@CNFs.

By thermogravimetric analysis (TG), the content of MnO QDs in the composite is calculated to be about 66 wt.% as shown in Fig. 3a. The

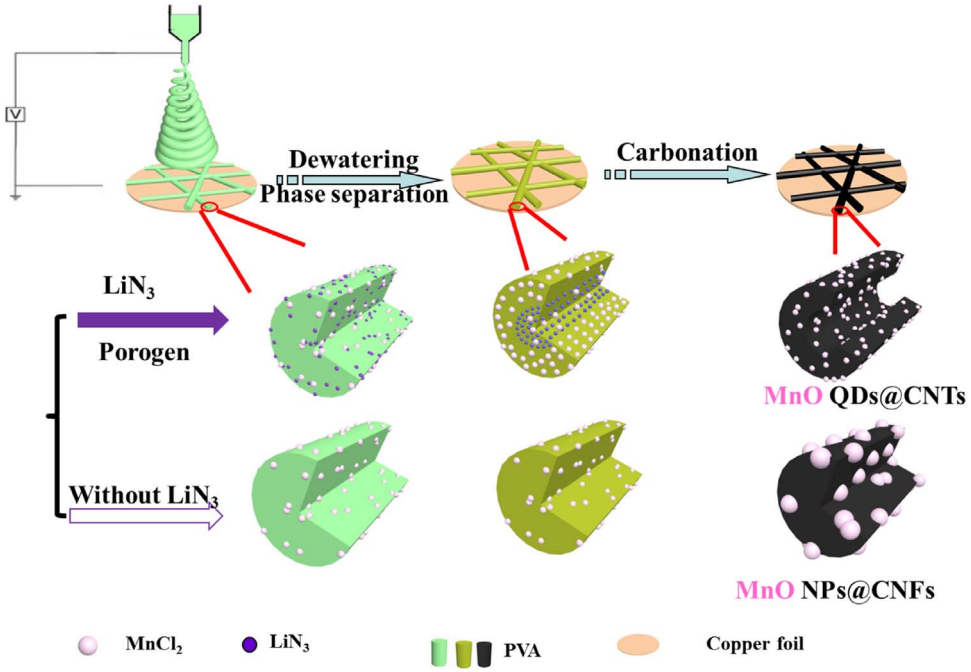

Fig. 1. Schematic illustration of fabricating MnO QDs@CNTs and MnO NPs@CNFs.

porous texture of MnO QDs@CNTs was further investigated by nitrogen adsorption/desorption isotherm at 77 K as shown in Fig. 3b. It revealed a specific surface area 65.2 $m^2 g^{-1}$ with a pore volume of 0.26 $cm^3 g^{-1}$. The distribution of Barrett – Joyner – Halenda (BJH) pore sizes (inset of Fig. 3b) was determined from the adsorption branch peaks at 20 and 75 nm, which confirms the porous characteristics of the MnO QDs@CNTs and corresponds well with that of SEM/TEM observations. The high specific surface area and the nanoporous texture of the MnO QDs@CNTs composite have advantages in lithium ion and electron transport. From X-ray diffraction (XRD) characterization, the structural information about the MnO QDs@CNTs was obtained. Fig. 3c displays the typical XRD patterns of MnO QDs@CNTs in which the characteristic peaks can be ascribed to a pure cubic phase of MnO, which agrees well with the SAED result [31] while no obvious peaks indexed to carbon was observed, which indicates the nature of amorphous carbon. Fig. 3c also shows the characteristic peak located at about 25°, which agrees well with the (002) plane of graphite. Additionally, the low intensity of it suggested the low degree of graphitization and the randomness of the structure. The disorder structure of MnO QDs@CNTs could be further confirmed by Raman spectroscopy. The Raman spectra in Fig. 3d shows that two obvious peaks located at 1342 and 1591 cm^{-1}, corresponding to the disordered carbon (D-band) [32] and the ordered graphitic carbon (G-band) [32,33], respectively. Furthermore, the intensity ratio of D band and G band (I_D/I_G) is calculated to be 1.05, suggesting the presence of abundant defects and vacancies in the as-formed CNTs [34], which not only benefit for the diffusion of lithium ions, but also provides more reversible sites for Li storage [8]. The electronic state on the surface and the composition of the products were analyzed by the X-ray photoelectron spectroscopy (XPS). The peaks arising from Mn (2 s, 2p) and O (1 s) in the survey XPS spectrum can be assigned to MnO as shown in Fig. 3e. Meanwhile [14], the peak labeled C 1 s originates from the carbon matrix. Further analysis of the Mn 2p peak was examined by high-resolution XPS as shown in Fig. 3f. The two signals at 641.9 and 654.1 eV could be attributed to Mn(II)$2p_{3/2}$ and Mn(II) $2p_{1/2}$, the characteristic of MnO, respectively [35].

For the sake of isolating the effect of the porogen LiN_3 on the formation of Mn QDs@CNTs, a control experiment without LiN_3 in the initial spinning solutions was carried out. The as-spun NFs (Fig. S5†) are similar to the samples spun with LiN_3 (Fig. 2a) while the morphology of the calcined products is quite different from MnO QDs@CNTs, where the MnO NPs with size about 40–50 nm uniformly distributed in the carbon nanofibers formed, marked as MnO NPs@CNFs, as shown in Figs. 2g and 2h. These results suggest that the introduced porogen LiN_3 is critical for the formation of the MnO QDs and the nanotube structures. XRD pattern as shown in Fig. S6† discloses that the as-prepared MnO NPs@CNFs is also pure cubic phase MnO, implying that LiN_3 has no effect on the compositions of the resultant products. Furthermore, the MnO NPs@CNFs shows a BET surface area of 5.8 $m^2 g^{-1}$ as shown in Fig. S7†, which is about 10 times lower than that of MnO QDs@CNTs (65.2 $m^2 g^{-1}$). These comparisons unambiguously suggest that (i) the porogen LiN_3 plays a critically pivotal role on the development of MnO QDs and CNTs, (ii) the porogen LiN_3 significantly enhances the BET surface area of the resultant fibers. Based on the described experiments and observations, a possible formation mechanism of MnO QDs@CNTs could be explained as follows. The mixed solutions containing deionized water, PVA, $MnCl_2$ and LiN_3 were spun on a copper foil. The metal oxide precursor $MnCl_2$ in the water environment will hydrolysis into $Mn(OH)_2$. During the electrospinning and drying steps, deionized water evaporates gradually [36] from the surface of nanofibers and the solvent concentration gradient along the direction of radius is formed [37], which cause the phase separation between the solution and polymer as shown in the schematic illustration in Fig. 1 [38]. As a result the LiN_3 concentrations in the center of the nanofibers are higher than that of near the surface due to the difference solubility of LiN_3 in water and polymer [39]. In the carbonization step, with the increase of temperature, the $Mn(OH)_2$ will decompose to MnO and the porogen LiN_3 will decompose into vapor phases to drive the MnO embedded in the carbon matrix to the shell region. At the same time, attributed to the separator function of soft carbonaceous shell and the N_2 released from the LiN_3 decomposition, the MnO nanocrystals can be prevented from agglomerating into larger particles [19]. After the LiN_3 in the core region decomposes completely, nanotubes with MnO QDs embedded in the carbon shell are prepared.

When considered for the application in lithium storage, in association with the unique 1D nanostructure with porous nanotube structure, MnO QDs@CNTs with such a ultra-uniform distribution is expected to

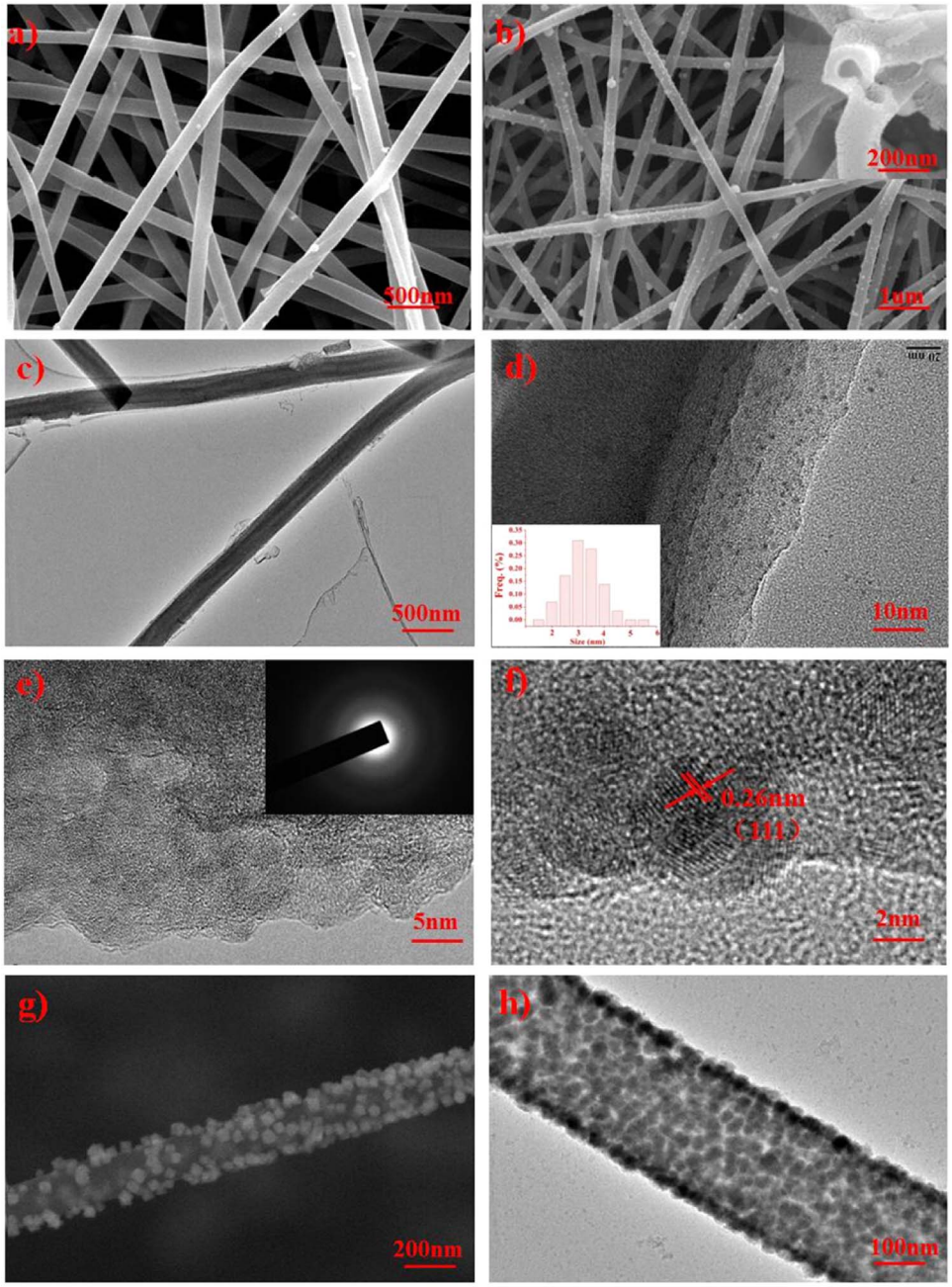

Fig. 2. Typical SEM images of the as-electrospun NFs (a) and the obtained MnO QDs@CNTs after carbonize (b). TEM (c, d) and HRTEM (e, f) images of MnO QDs@CNTs under different magnifications. Typical SEM (g) and TEM (h) images of the obtained MnO NPs@CNFs. (Inset: the cross section (b), size distribution (d) and SAED (e) of MnO QDs@CNTs).

exhibit high capacity and excellent performance. To confirm it, MnO QDs@CNTs were selected and measured as a typical sample of electroactive materials in LIBs in detail. It is noted that the capacity is calculated based on the total mass of the materials containing carbon nanotubes and MnO QDs. Fig. 4a shows the typical cyclic voltammograms (CVs) of MnO QDs@CNTs electrode in the initial three cycles at a scan rate of 0.1 mV s^{-1} between 0 and 3 V at room temperature. A peak centered at about 0.24 V is attributed to the reduction of manganese oxide to metallic manganese, in the first cathodic polarization process, and the formation of Li_2O and another cathodic peak located at about 0.74 V corresponds to the decomposition of electrolyte and the formation of solid electrolyte interface (SEI) layer on the surface of electrode materials [16]. The peak located at 1.26 V in the first anodic sweep corresponds to the oxidation of manganese. Apparently, both in the second and third cycles, the main cathodic peak shifts to about 0.42 V, indicating that the lithiation voltage (≈0.42 V) is higher than that in the first cycle (≈0.24 V), which is due to the enhanced kinetics of the MnO QDs@CNTs electrode arising from the microstructure alteration and formation of Li_2O and mental Mn after the first lithiation process [28]. In addition, the CV curve of the third scan is slightly different from that of the second one. The voltage profiles of different cycles for the as formed MnO QDs@CNTs electrode at a current density of 100 mA g^{-1} are shown in Fig. 4b. The potential plateau in range of 0.5–0.75 V corresponds to the lithiation process while that in 1.1–1.3 V corresponds to the delithiation, coinciding well with the CV curves. The first discharge and charge capacities of the MnO QDs@CNTs electrode are 3168 and 1669 mAh g^{-1} respectively. The large capacity loss in the first cycle is mainly attributed to the irreversible processes such as electrolyte decomposition and inevitable formation of the SEI layer [16]. Secondly, 50th and 80th cycles, the discharge capacities are 1728, 1083 and 1088 mAh g^{-1}, respectively, much higher than the theoretical capacities of both MnO

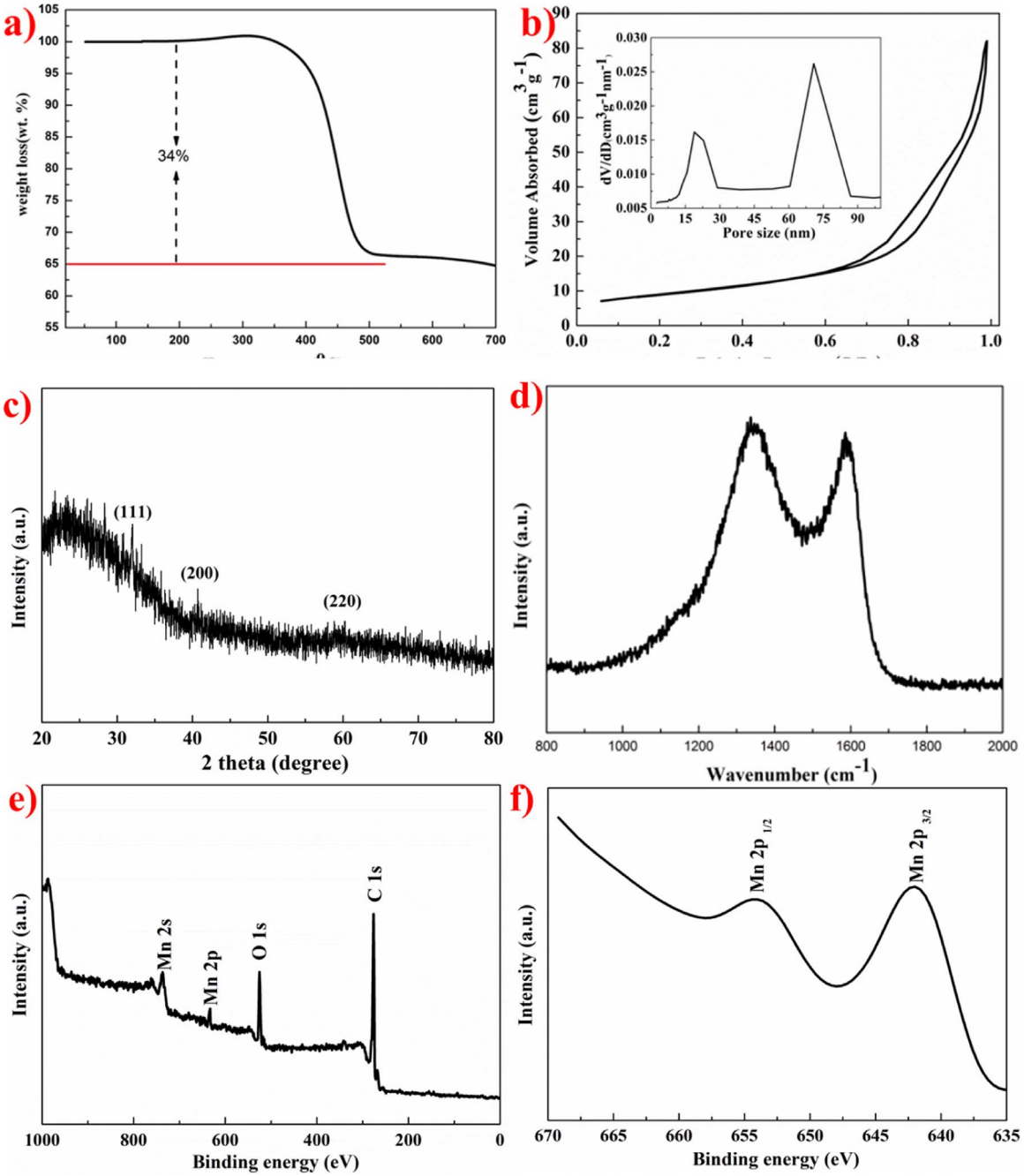

Fig. 3. TG curve (a), N2 sorption isotherms and pore size distributions (b), XRD patterns (c), Raman spectrum (d), XPS spectra (e and f) of MnO QDs@CNTs composite (survey spectrum (e), high-resolution of Mn 2p (f)).

(756 mAh g^{-1}) and carbon (374 mAh g^{-1}). The electrode delivers a stable capacity of 1100 mAh g^{-1} after the first 5 cycles, and the coulombic efficiency of the electrode is maintained around 100% in the following cycles as shown in Fig. 4c. An excellent cycling performance plays an important role in promising anode materials. In this case, the MnO QDs@CNTs electrode is cycled at high current densities to investigate the long-life performance. For the comparison of MnO QDs@CNTs, MnO NPs@CNFs and bulk MnO, Fig. 4d shows the discharge capacity versus cycle number at a constant rate of 3000 mA g^{-1}. Obviously, the MnO QDs@CNTs electrode has much better cycling stability. After about 20 cycles, it delivers a stable discharge capacity of 534 mAh g^{-1}, whereas that of the MnO NPs@CNFs electrode and bulk MnO are just 348 and 92 mAh g^{-1}, respectively. The MnO QDs@CNTs electrode can still reach 603 mAh g^{-1} in capacity with slight increase even after 200 cycles. This phenomenon is probably associated with either the formation of the SEI films or the high oxidation-state product, as demonstrated in recent reports on MnO-based materials for LIBs [14]. By comparison, a discharge capacity of only 344 and 45 mAh g^{-1} can be obtained for MnO NPs@CNFs and bulk MnO in the same condition. Furthermore, as shown in Fig. 4e, the MnO QDs@CNTs electrodes exhibit satisfactory rate performance. Firstly, The nanocomposites are tested at the same charge and discharge current densities of 100 mA g^{-1}, and then current densities are increased from 100 to 3000 mA g^{-1}. The MnO QDs@CNTs deliver a high average capacity of 1295 mAh g^{-1} at 100 mA g^{-1}. Even when measured at a very high current density of 3000 mA g^{-1}, a large capacity of 620 mAh g^{-1} can still be obtained. After deeply charge/discharge for 5 cycles at 3000 mA g^{-1}, an average capacity of 1040 mAh g^{-1} is recovered when scanned again at 100 mA g^{-1}. As comparisons, the MnO NPs@CNFs and bulk MnO exhibit lower

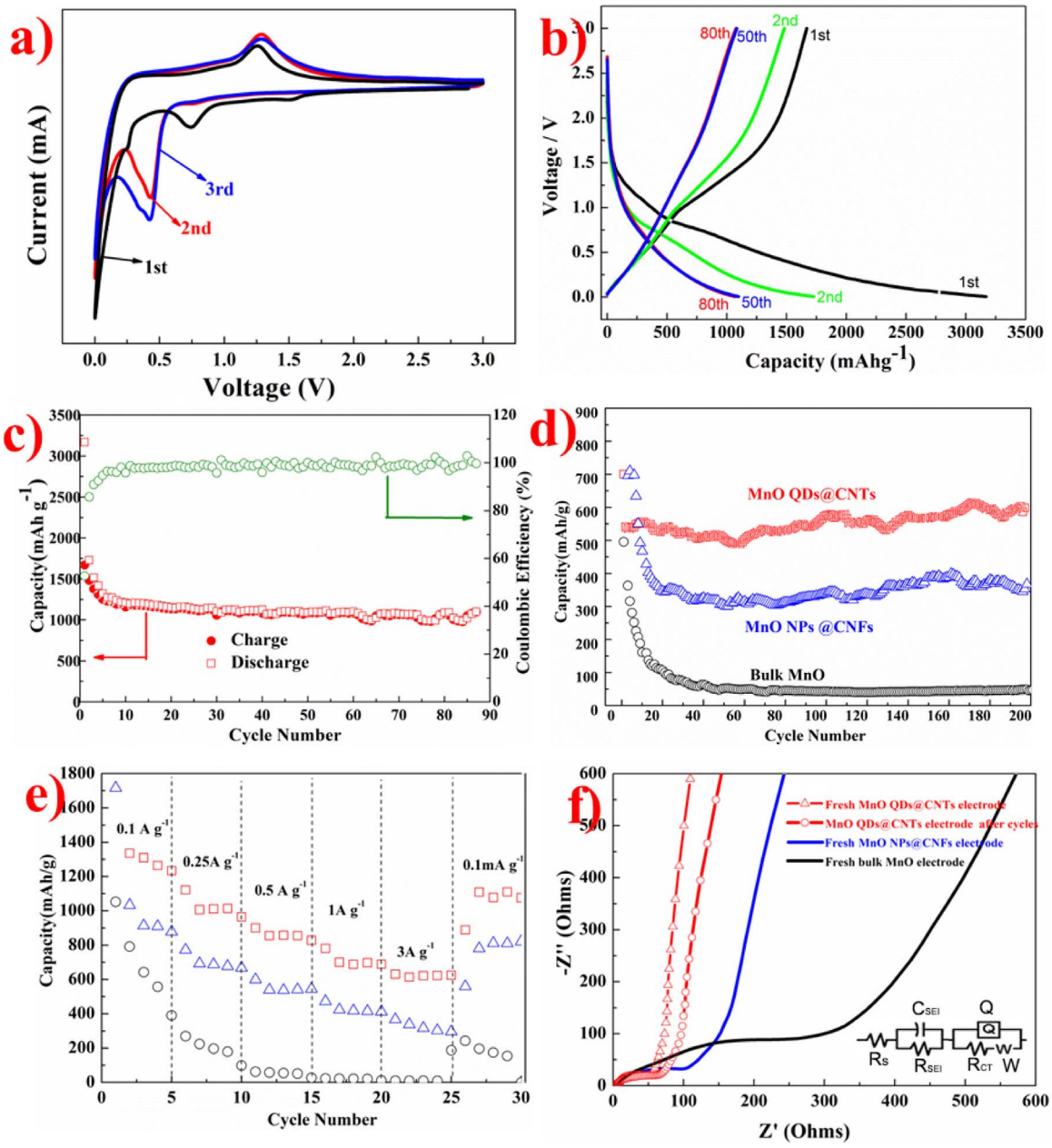

Fig. 4. (a) CV curves of MnO QDs@CNTs in the potential range from 3.0 to 0.01 V vs Li/Li$^+$. (b) Charge – discharge curves of MnO QDs@CNTs at 100 mA/g for different cycles. (c) Cycling performance of MnO QDs@CNTs at 100 mA g^{-1}. (d) Cycling performance of MnO QDs@CNTs, MnO NPs@CNFs and bulk MnO at 3000 mA g^{-1}. (e) Rate performance of MnO QDs@CNTs, MnO NPs@CNFs and bulk MnO. (f) AC Impedance plots for MnO QDs@CNTs, MnO NPs@CNFs and bulk MnO and MnO QDs@CNTs after 200 cycles at 3000 mA g^{-1} (Inset: the equivalent circuit).

capacities of 297.3 and 15.7 mAh g^{-1} at a current density 3000 mA g^{-1}, with poor rate capability. The outstanding properties indicate that the lithium ions can rapidly insert and extract from the active materials and retain a stable structure even after continuous discharge/charge cycles.

The electrochemical impedance spectroscopy (EIS) measurements on the electrodes of MnO QDs@CNTs, MnO NPs@CNFs and bulk MnO powders before cycling and after 200 cycles were also performed to gain deeper insights into the remarkable enhanced electrochemical reaction kinetics and cycling performance of MnO QDs@CNTs. In the electrochemical impedance spectra (Fig. 4f), the depressed semicircle at high frequency belongs to the Nyquist plot which is relevant to the charge transfer reaction at the electrolyte/electrode interface, while the linear Warburg part at the low frequency represents the diffusion of the lithium ions in the bulk of the electrode. The related equivalent circuits of MnO QDs@CNTs is given (the inset of Fig. 4(f)) to calculate the resistances of electrodes, in which R_S represents the resistance related to the conductivity of electrolyte, active material and current collector, R_{SEI} and C_{SEI} reflect the resistance of the active particles passing the SEI film and the corresponding capacitance, RCT, Q and W represent resistance related to charge-transfer, constant phase elements, and Warburg impedance associated with Li-ion diffusion, respectively. The fitting curve estimated by the equivalent circuit coincides well with the experimental one (Fig. S8†). The fresh MnO QDs@CNTs electrode demonstrates a lowest resistance of about 60 Ω compared to the MnO NPs@CNFs (130 Ω) and bulk MnO (400 Ω) electrode. Such a reduction is owing to the unique combination of ultra-small MnO QDs and excellent transport properties of CNTs, boosting the Li$^+$ reaction kinetics. Additionally, the electrochemical impedance spectrum of the MnO QDs@CNTs after 200 cycles at 3000 mA g^{-1} was also measured, just a slight increase compared to that before cycling, further suggesting the high structural integrity [40]. Compared with those previously

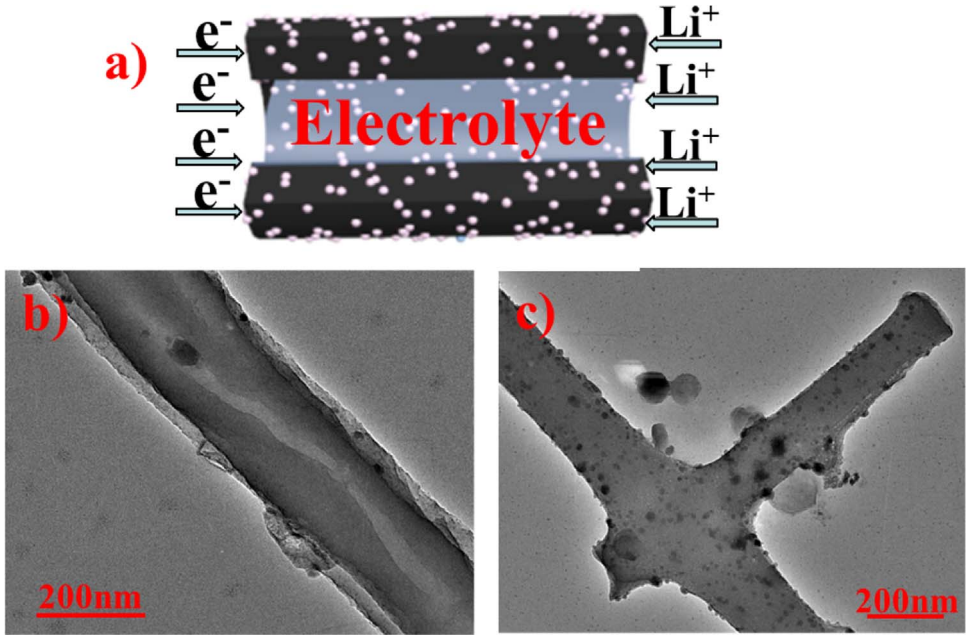

Fig. 5. (a) Schematic representation showing paths for lithium-ions and electrons in the MnO QDs@CNFs. (b) TEM image of a single MnO QDs@CNTs after 200 cycles at 3000 mA g^{-1}. (c) TEM image of MnO NPs@CNFs after 200 cycles at 3000 mA g^{-1}.

reported manganese oxide/carbonaceous hybrid materials (Table S1†), the MnO QDs@CNTs electrode shows great potential as an anode in practical applications, with competitive reversible capacity.

The excellent electrochemical properties exhibited in the present MnO QDs@CNTs electrode can be explained as the following reasons. Firstly, the small particle size and uniform distribution of MnO QDs are the key factors for the composites to achieve high electrochemical performances. As shown in Fig. 5a, short ion-diffusion length is achieved by the ultra-small MnO QDs, which will facilitate the full utilization of the active material even at high scan rate [26]. Secondly, the nanotubes with porous walls have more active reaction sites caused by higher surface area, shorter diffusion paths for both lithium ions and electrons providing faster redox reactions [41]. Thirdly, the electrodes integrity is also considered to be an important factor in maintaining good cycle stability [42]. NFs arising from electrospinning could be woven into a network resulting that the nanofibers connect with each other very well for the fast transfer of electrons leading to low resistance of the electrode [43]. Finally, the carbon matrices not only prevented the aggregation of MnO QDs, but also avoided the exfoliation of MnO QDs during cycling lithiation/delithiation process, maintaining the integrity of the whole electrode. The direct evidence is from the TEM image (Figs. 5b, 5c) of MnO QDs@CNTs and MnO NPs@CNFs after over 200 cycles at 3000 mA g^{-1}. It shows that the MnO QDs@CNTs morphology has been well maintained after long term stability test. Furthermore, good conductivity can be realized for the composite because the carbon shell is a good electronic conductor. All of these facts make MnO QDs@CNTs a anode material for practical applications with great promise.

4. Conclusions

In summary, the MnO QDs embedded in CNTs have been constructed by scalable and facile electrospinning method with a porogen LiN_3 and further evaluated as an anode material for rechargeable Li-ion batteries. With the combination of ultrasmall MnO NPs (3~4 nm), uniform distribution and porous CNTs structure, MnO QDs@CNTs composite rendered outstanding electrochemical performance as an anode of LIBs, in terms of reversible specific capacity and cycling stability, especially where a capacity of about 603 mAh g^{-1} at much high current density of 3000 mA g^{-1} after 200 cycles has been realized. These results would shed light on the practical application of MnO-based materials as a high capacity electrode with high rate capability for next-generation energy storage and other applications.

Acknowledgements

This work was partially supported by the National Natural Science Foundation of China (51471053 and 51625102).

Appendix A. Supplementary material

Supplementary data associated with this article can be found in the online version at doi:10.1016/j.ensm.2017.01.007.

References

[1] B. Dunn, H. Kamath, J.-M. Tarascon, Science 334 (2011) 928–935.
[2] K. Zhang, X. Han, Z. Hu, X. Zhang, Z. Tao, J. Chen, Chem. Soc. Rev. 44 (2015) 699–728.
[3] M.-H. Park, M.G. Kim, J. Joo, K. Kim, J. Kim, S. Ahn, Y. Cui, J. Cho, Nano Lett. 9 (2009) 3844–3847.
[4] X. Gu, L. Chen, Z. Ju, H. Xu, J. Yang, Y. Qian, Adv. Funct. Mater. 23 (2013) 4049–4056.
[5] H.J. Qiu, L. Liu, Y.P. Mu, H.J. Zhang, Y. Wang, Nano Res. 8 (2015) 321–339.
[6] S.H. Choi, J.-K. Lee, Y.C. Kang, Nano Res. 8 (2015) 1584–1594.
[7] K.Z. Cao, L.F. Jiao, Y.C. Liu, H.Q. Liu, Y.J. Wang, H.T. Yuan, Adv. Funct. Mater. 25 (2015) 1082–1089.
[8] A.L.M. Reddy, M.M. Shaijumon, S.R. Gowda, P.M. Ajayan, Nano Lett. 9 (2009) 1002–1006.
[9] H. Jiang, Y. Hu, S. Guo, C. Yan, P.S. Lee, C. Li, ACS Nano 8 (2014) 6038–6046.
[10] J. Guo, Q. Liu, C. Wang, M.R. Zachariah, Adv. Funct. Mater. 22 (2012) 803–811.
[11] Y. Xia, Z. Xiao, X. Dou, H. Huang, X. Lu, R. Yan, Y. Gan, W. Zhu, J. Tu, W. Zhang, X. Tao, ACS Nano 7 (2013) 7083–7092.
[12] Y.R. Zhong, M. Yang, X.L. Zhou, Y.T. Luo, J.P. Wei, Z. Zhou, Adv. Mater. 27 (2015) 806–812.
[13] H. Wang, L.-F. Cui, Y. Yang, H. Sanchez Casalongue, J.T. Robinson, Y. Liang, Y. Cui, H. Dai, J. Am. Chem. Soc. 132 (2010) 13978–13980.
[14] Y. Sun, X. Hu, W. Luo, F. Xia, Y. Huang, Adv. Funct. Mater. 23 (2013) 2436–2444.
[15] H. Liu, Z.H. Li, Y.R. Liang, R.W. Fu, D.C. Wu, Carbon 84 (2015) 419–425.
[16] Z.Y. Cai, L. Xu, M.Y. Yan, C.H. Han, L. He, K.M. Hercule, C.J. Niu, Z.F. Yuan, W.W. Xu, L.B. Qu, K.N. Zhao, L.Q. Mai, Nano Lett. 15 (2015) 738–744.
[17] K. Zhong, B. Zhang, S. Luo, W. Wen, H. Li, X. Huang, L. Chen, J. Power Sources 196 (2011) 6802–6808.
[18] A.S. Arico, P. Bruce, B. Scrosati, J.M. Tarascon, W. Van Schalkwijk, Nat. Mater. 4 (2005) 366–377.
[19] L. Su, Y. Zhong, J. Wei, Z. Zhou, RSC Adv. 3 (2013) 9035–9041.
[20] S.J. Yang, S. Nam, T. Kim, J.H. Im, H. Jung, J.H. Kang, S. Wi, B. Park, C.R. Park, J.

Am. Chem. Soc. 135 (2013) 7394–7397.
[21] D.I. Son, B.W. Kwon, D.H. Park, W.-S. Seo, Y. Yi, B. Angadi, C.-L. Lee, W.K. Choi, Nat. Nanotechnol. 7 (2012) 465–471.
[22] J.M. Caruge, J.E. Halpert, V. Wood, V. Bulovic, M.G. Bawendi, Nat. Photonics 2 (2008) 247–250.
[23] P.L. Feng, J.J. Perry, S. Nikodemski, B.W. Jacobs, S.T. Meek, M.D. Allendorf, J. Am. Chem. Soc. 132 (2010) 15487–15489.
[24] Z. Zhu, S. Wang, J. Du, Q. Jin, T. Zhang, F. Cheng, J. Chen, Nano Lett. 14 (2014) 153–157.
[25] C. Han, M. Yan, L. Mai, X. Tian, L. Xu, X. Xu, Q. An, Y. Zhao, X. Ma, J. Xie, Nano Energy 2 (2013) 916–922.
[26] G. Zhang, J. Zhu, W. Zeng, S. Hou, F. Gong, F. Li, C.C. Li, H. Duan, Nano Energy 9 (2014) 61–70.
[27] G. Zhang, S. Hou, H. Zhang, W. Zeng, F. Yan, C.C. Li, H. Duan, Adv. Mater. 27 (2015) 2400–2405.
[28] H. Xia, C. Hong, B. Li, B. Zhao, Z. Lin, M. Zheng, S.V. Savilov, S.M. Aldoshin, Adv. Funct. Mater. 25 (2015) 627–635.
[29] R. Mo, Z. Lei, K. Sun, D. Rooney, Adv. Mater. 26 (2014) 2084–2088.
[30] C. Zhu, D. Chao, J. Sun, I.M. Bacho, Z. Fan, C.F. Ng, X. Xia, H. Huang, H. Zhang, Z.X. Shen, G. Ding, H.J. Fan, Adv. Mater. Interfaces 2 (2015) 1400499.
[31] Y.J. Mai, D. Zhang, Y.Q. Qiao, C.D. Gu, X.L. Wang, J.P. Tu, J. Power Sources 216 (2012) 201–207.
[32] L. Ji, X. Zhang, Nanotechnology 20 (2009) 155705.
[33] L. Qie, W. Chen, H. Xu, X. Xiong, Y. Jiang, F. Zou, X. Hu, Y. Xin, Z. Zhang, Y. Huang, Energy Environ. Sci. 6 (2013) 2497–2504.
[34] Z.-S. Wu, W. Ren, L. Xu, F. Li, H.-M. Cheng, Acs Nano 5 (2011) 5463–5471.
[35] V. Dicastro, S. Ciampi, Surf. Sci. 331 (1995) 294–299.
[36] X.H. Li, C.L. Shao, Y.C. Liu, Langmuir 23 (2007) 10920–10923.
[37] C. Gao, X. Li, B. Lu, L. Chen, Y. Wang, F. Teng, J. Wang, Z. Zhang, X. Pan, E. Xie, Nanoscale 4 (2012) 3475–3481.
[38] J. Kong, H.R. Tan, S.Y. Tan, F. Li, S.Y. Wong, X. Li, X. Lu, Chem. Commun. 46 (2010) 8773–8775.
[39] J. Fu, J. Zhang, C. Zhao, Y. Peng, X. Li, Y. He, Z. Zhang, X. Pan, N.J. Mellors, E. Xie, J. Alloy. Compd. 577 (2013) 97–102.
[40] Y. Zhang, P. Chen, X. Gao, B. Wang, H. Liu, H. Wu, H. Liu, S. Dou, Adv. Funct. Mater. 26 (2016) 7754–7765.
[41] H.S. Oktaviano, K. Yamada, K. Waki, J. Mater. Chem. 22 (2012) 25167–25173.
[42] M. Zhang, E. Uchaker, S. Hu, Q.F. Zhang, T.H. Wang, G.Z. Cao, J.Y. Li, Nanoscale 5 (2013) 12342–12349.
[43] M. Zhang, F.L. Yan, X. Tang, Q.H. Li, T.H. Wang, G.Z. Cao, J. Mater. Chem. A 2 (2014) 5890–5897.